Controlled defects to link wetting properties to surface heterogeneity

Romain Lhermerout, Kristina Davitt

Soft Matter

ARTICLE TYPE

Cite this: DOI: 10.1039/xxxxxxxxxx

Controlled defects to link wetting properties to surface heterogeneity†

Romain Lhermerout[a] and Kristina Davitt*[a]

Received Date
Accepted Date

DOI: 10.1039/xxxxxxxxxx

www.rsc.org/journalname

Small-scale heterogeneities have long been understood to give rise to contact angle hysteresis. More recently, the question of how they influence contact line dynamics has generated interest. Models that express the hysteresis or dynamics in terms of defect properties exist but have yet to be conclusively tested by experiment. Here we produce heterogeneous surfaces and thoroughly characterize individual defects. Precise dynamical measurements allow us to conclude that there is no evidence of a thermally-activated dynamics due to their presence, but that the hysteresis scales with their concentration and the square of their height, as predicted by some simple models.

1 Introduction

Defects or inhomogeneities on a solid surface affect how a liquid front moves over the surface. This is most readily seen in the contact angle hysteresis: the angle that the edge of a drop makes with the underlying surface depends on the direction in which the drop is moving. This arises from the ability of defects to pin the three-phase contact line, thus necessitating a minimum force to overcome the pinning and for the drop to move. In their pioneering work, Joanny and de Gennes developed a simple model to express the balance between the pinning force of a individual chemical or topographical defect and the elastic restoring force of the deformed contact line and then related it to the macroscopic contact angle hysteresis in the case of non-interacting defects[1]. Although originally formulated for scales beyond that where van der Waals interactions are important, this model has recently been shown[2] to describe the pinning on nano-defects with pinning energies of the order of $k_B T$. Further models and numerical studies[3] have investigated collective effects arising from the interaction between defects. Although hysteresis is readily observed, only a few experimental studies have attempted to show that model predictions are consistent with properties of the individual, microscopic or nanoscopic defects[2,4–8], or exploited its variation with concentration to investigate collective effects[9,10]. Systematic experiments to determine the scaling on defect parameters are lacking and which, if any, models are applicable to any given real surface remains therefore to be fully tested.

Contact angle hysteresis is easily observed in everyday phenomena, such as the asymmetry of a drop slowly sliding down a vertical wall or stuck inside a straw. How defects affect the full dynamics of the contact line is less evident to the naked eye. This can be characterized by measuring the variation of the contact angle with the velocity of the contact line. A few experiments[11–14] have attempted to quantify how measurable surface properties affect the obtained dynamics. The task is not simple as the motion of the contact line on the background reference surface (i.e. without additional defects) exhibits its own dynamics, and in addition, experiments may access multiple dynamical regimes, each of which may be influenced differently by the presence of defects. For example, at high capillary number one expects viscous effects to be important, whereas at low velocities the motion may be dominated by thermally activated pinning and depinning on molecular or nanoscale imperfections. Indeed, even without explicitly added defects, it is an outstanding question of how to describe the full range of dynamics. Some attempts have been made to account for both viscous dissipation and activated dynamics[8,15,16], including by ourselves[17,18], where we propose a unified description of these regimes and extend the static model of Joanny and de Gennes to account for thermal activation. Although the situation is not yet clear, consensus is that —provided the energy barriers to motion created by defects are small enough— the slope of the dynamics in the activated regime will reflect characteristics of the defects. To answer the question of how defects affect the dynamics, it is therefore necessary to have an understanding of the dynamics on the reference surface, and then to compare the regime at lowest capillary numbers to that on surfaces containing well-characterized defects.

In this paper we produce and characterize purely topographical defects with continuously varying size, shape and density and measure the dynamics for each with several different liquids. We use a reference surface that presents a minuscule background hys-

[a] Laboratoire de Physique Statistique (LPS), UMR 8550 CNRS, ENS, Univ. Paris Diderot, Sorbonne Université, 24 rue Lhomond, 75005, Paris, France. E-mail: kristina.davitt@lps.ens.fr

† Electronic Supplementary Information (ESI) available: [details of any supplementary information available should be included here]. See DOI: 10.1039/cXsm00000x/

teresis and whose dynamics has been understood [19]. We find that the presence of defects has no effect on the slopes of the dynamics, even for defects with estimated energy barriers of the order of $100\,k_BT$. The presence of defects only separates the advancing (A) and receding (R) branches of the dynamics, i.e. controls the hysteresis, which we define here as

$$H = \gamma(\cos\theta_R - \cos\theta_A), \tag{1}$$

where γ is the liquid-vapor interfacial tension and the angles are measured at a low enough velocity such that viscous effects are negligible. We find that H varies linearly with the density of defects for all cases studied, from which an energy dissipated per defect can be determined; here ranging from 100 to $10^5\,k_BT$. Further, for the spherical cap and Gaussian-shaped defects used here, H is found to scale as the square of the defect height. First we follow previous studies in comparing to the original model based on strong independent defects [1] and find that experimental results agree well with the simple scaling derived from this model, even in the case of weak and dense defects, that is, outside of the range of validity of the model. We suggest that the physical mechanism responsible for the observed hysteresis has therefore not been fully understood and call for further numerical work to simulate the hysteresis on surfaces covered with defects of known properties (such as the defect shape and concentrations measured herein) to evaluate the importance of other mechanisms such as collective effects or the existence of a force threshold even for independent weak defects.

2 Experiment

2.1 Obtaining defects

The purpose of this study is to link macroscopic wetting properties —the dynamics and hysteresis— to the heterogeneity of the underlying solid surface at microscopic scales. It is therefore necessary to have control over individual defects. They should be large enough that they are easily characterized by standard microscopy tools, but small enough that their associated energy barriers are comparable to thermal energy such that it is conceivable to measure a regime of thermally-activated motion, if it is indeed present. This is a question of resolution in the measurement of the dynamics.

Activated motion is the contact line moving from one local energy minimum to another by thermal fluctuations and can be modeled by an Arrhenius process. In the simplest form, it yields a velocity v (or capillary number Ca) that depends exponentially on the distance of the cosine of the dynamic angle from the equilibrium one:

$$|\mathrm{Ca}| = \left|\frac{\eta v}{\gamma}\right| = \mathrm{Ca}_0 \exp\left[\frac{\gamma\lambda^2}{2k_BT}\left|\cos\theta - \cos\theta_{eq}\right|\right], \tag{2}$$

where η is the liquid viscosity, γ the liquid-vapor interfacial tension, k_B is Boltzmann's constant and T is the temperature. Here λ is referred to as the activation length and Ca_0 as the transition capillary number [18], which has also sometimes been related to the thermal attempt frequency [20]. If the dynamics is truly activated, then the activation length can be found from the slopes of experimental curves plotted on a semi-logarithmic scale (for example, see Fig. 2):

$$\left|\frac{\mathrm{d}\log|\mathrm{Ca}|}{\mathrm{d}\cos\theta}\right| = \frac{\gamma\lambda^2}{2k_BT\ln 10}. \tag{3}$$

In the experiments we describe below, a variation of about 0.01° over one decade in velocity can be detected. A typical equilibrium contact angle in this study is $\theta_{eq} \approx 15^\circ$. Assuming that the energy barrier to motion created by a single defect is of order $\gamma\lambda^2$, then eqn 3 gives a maximum energy barrier of $E_b \approx 5.10^4\,k_BT$ in order for an activated regime to be detectable. For simple liquids and assuming that λ is of the order of the defect dimension this implies that defects should be of the order of 100 nm or smaller.

We have achieved this by sintering silica nanospheres at different temperatures to obtain topographical bumps with different heights and slopes. The procedure has been borrowed from Ref.[21] and is only briefly outlined here. A piece of silicon wafer is cleaned in piranha solution then activated in oxygen plasma (30W, Harrick Plasma PDC-002) for 3 min. It is then immediately placed in a $1\,\mathrm{mg\,ml^{-1}}$ solution containing PEI polymer (polyethylenimine, Sigma-Aldrich) and left for 1 h. The adsorbed PEI layer is charged oppositely to the spheres; it adheres the spheres to the surface and minimizes the clustering of particles that occurs when a particle-containing liquid is dip-coated on a surface. After rinsing under deionized water, the sample is then stirred in a diluted solution of silica nanospheres. Although the stirring time and concentration of the nanosphere solution control the number density of spheres that are deposited in a predictable way [22], we nonetheless measure the density of beads on each sample by counting them under AFM. We count sufficiently many to ensure that the counting error is typically less than 3%. Unless otherwise stated, the nanospheres used in this study have a nominal diameter of 80 nm (Klebosol 30HB50K, AZ Electronic Materials, France). Samples are then placed in an oven (Nabertherm L5/13/B180) that ramps the temperature up in 2 h and holds it for another 2 h at final temperatures between 1080 °C and 1180 °C. This destroys the PEI layer, causes a thick silicon oxide to form on the bare parts of the wafer, and sinters the silica nanospheres, as illustrated in Fig. 1. The final height h_0 and shape profiles of the sintered beads are obtained by AFM. The resulting surface is thus chemically homogeneous (silicon oxide) but has topographical bumps of known shape and density. Figure 1 shows a typical distribution and example shapes of the obtained defects. We have verified that the molecular coating described below has a negligible effect on the size and shape of the defects formed from sintered 80 nm nanospheres [23].

2.2 The reference surface

A reference surface that exhibits hysteresis indicates that there are heterogeneities present even in absence of explicitly added nanospheres. This raises the specter of competition or of collective behavior between the two classes of defects and complicates the interpretation of which microscopic parameters control the hysteresis and dynamics. To minimize this possibility, we aim to use a reference surface with minimal intrinsic hysteresis. We have therefore deposited a PDMS pseudo-brush on the silicon ox-

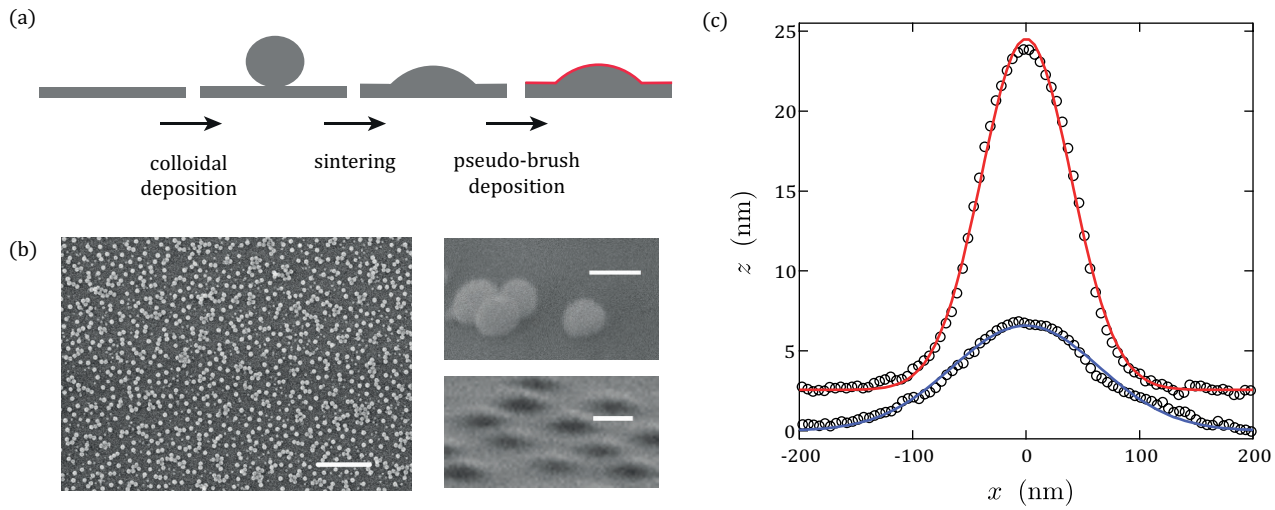

Fig. 1 (a) Schematic illustration of the procedure to fabricate controlled defects. (b) SEM images of the produced surfaces illustrating (left, scale bar $1\,\mu$m) the homogeneity in coverage even for high concentrations (here $n = 35\,\mu\text{m}^{-2}$) and the shapes (right, scale bars 100 nm) with little (1080 °C) or considerable (1164 °C) sintering. (c) Example height profiles of sintered defects obtained by AFM. Red and blue lines are fits to eqn 5 for sintering temperatures of 1144 °C and 1164 °C respectively. The former curve has been shifted upwards for clarity.

ide surface, as illustrated in Fig. 1. PDMS pseudo-brushes have been reported to show exceptionally low hysteresis and they are very easily produced[24,25]. We have recently shown[19] that the contact line dynamics of good solvents, such as alkanes, on such surfaces is dominated by a visco-elastic dissipation that depends on the polymerization index of PDMS used to create the brush, with hydrodynamic dissipation kicking in at capillary numbers above roughly $\text{Ca} \approx 10^{-7}$. In the work reported here, we exclusively use PDMS with a polymerization index of N=126, which yield pseudo-brush layers about 4 nm thick. For decane on such a reference surface we find a contact angle hysteresis of the order of 0.1° for velocities below $10\,\mu\text{m s}^{-1}$ (red curve in Fig. 2), which is better than the hysteresis observed on other molecular-scale coatings such as carefully produced self-assembled monolayers of thiols or silanes, while being much easier to obtain reproducibly. The hysteresis with water is roughly 10° at $10\,\mu\text{m s}^{-1}$ or nearly 2° at the minimum velocities we can attain.

2.3 Wetting measurements

We use a custom-built dip-coating apparatus to measure contact line dynamics. The principle is straightforward, and exhaustive details have been published elsewhere[26]. As illustrated in the inset of Fig. 2, the sample is plunged into, or retracted from, a liquid bath at a velocity controlled by either a motorized or piezo-driven stage. The dynamic contact angle θ is obtained by examining the capillary rise z_{cap} under microscope and from the following relation:

$$z_{\text{cap}} = \sqrt{\frac{\gamma}{\rho g}}\sqrt{1-\sin\theta} \qquad (4)$$

where ρ is the liquid density and g is the standard acceleration due to gravity. Here we report measurements made with decane, hexadecane or water. The liquid properties used in this study are given in Table 1. Since one aim of this work is to examine the possible existence of thermally-activated motion, it is necessary to measure the dynamics down to the lowest possible velocities. Care has been taken to minimize vibrations, temperature variation and evaporation, which are key to obtaining reliable dynamics at velocities down to as low as $1\,\text{nm s}^{-1}$. We are able to reach a precision of 0.01° in relative variations of the contact angle and about 1° in the absolute angle.

The contact angle hysteresis, defined in eqn 1, is determined here from the dynamic advancing and receding angles measured at a velocity of $10\,\mu\text{m s}^{-1}$.

Table 1 Liquid properties at 20 °C

liquid	γ(mN/m)	$\rho\,(10^3\text{kg m}^{-3})$	η (mPa s)	θ(°)
decane	23.83 [27]	0.7300 [28]	0.92 [28]	15
hexadecane	27.47 [27]	0.7733 [28]	3.34 [28]	33
water	72.88 [27]	0.9982 [29]	1.0016 [29]	106

3 Results and analysis

3.1 Dynamics

Figure 2 shows the contact line dynamics measured on the reference surface in the absence of any additional defects and the dynamics on a surface with nearly 1 nanosphere/μm^2. Here the defects are barely sintered (1080 °C, $h_0 = 74.1$ nm) and the liquid is decane. The dynamics are shown on a logarithmic scale, emphasizing the lowest velocities, where thermal activation may play a role.

Fits over the lowest four decades in velocity to eqn 3 yield activation lengths λ of order 100 nm for both the reference and the surface with defects. However, in the case of the former curve, in a previous study[19] we showed that the contribution coming from hydrodynamic dissipation is negligible below approximately $100\,\mu\text{m s}^{-1}$ and that the remaining dynamics can be entirely attributed to a visco-elastic dissipation in the thin PDMS layer. In other words, there is no evidence of thermal activation on the ref-

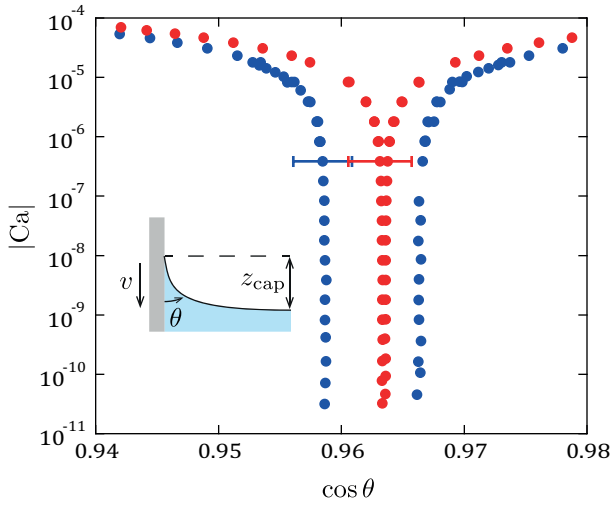

Fig. 2 Contact line dynamics measured on the reference surface (red symbols) and on a surface covered with defects (blue symbols) using decane. The defects were sintered at 1080 °C and have a concentration of $n = 0.8\mu\text{m}^{-2}$. Error bars shown on the data point taken at $10\mu\text{m s}^{-1}$ correspond to the uncertainty in the absolute angle. This is also the velocity at which the hysteresis is defined. Inset illustrates the capillary rise near a solid surface and the quantities defined in eqn 4.

erence surface. There is no detectable difference in slope when defects are added, from which we conclude that there is no evidence for activation over the defects either. One may ask if the defects and their energy barrier to motion are indeed small enough to generate a detectable thermal activation. As described in section 3.3 below, much shallower defects have also been produced, which, consequently, have a much lower energy barrier. Dynamics obtained in this case[†] show a much smaller hysteresis such that the two dynamical curves nearly overlap on the scale of Fig. 2. There is still no detectable change in the low-velocity slope.

3.2 Hysteresis and defect concentration

We prepared a series of samples with different defect concentrations for nanospheres sintered at two different temperatures. Three liquids were used for each: decane, hexadecane and water. Figures 3a and b show the hysteresis obtained from the separation of the advancing and receding branches of the dynamics at $10\mu\text{m s}^{-1}$. There is a fundamental question of where the usual quasi-static definition of the hysteresis is located on an experimental dynamical curve, a notion that we have recently attempted to clarify[18]. Here, however, since the slope of the dynamics does not change with the presence of defects, the precise choice of the velocity at which the hysteresis is defined is of little consequence: it can potentially add an constant offset to the absolute H but does not change the variation of H (from sample to sample), which is what we will use in the following.

Highly sintered spheres result in nearly Gaussian-shaped defects with a width of $2d = 130\,\text{nm}$, as seen in the AFM profiles in Fig. 1c. Figure 3a shows that the hysteresis scales linearly with the defect concentration n for the two alcanes, up to the highest concentrations tested. This corresponds to very dense coverage since the defects are separated by about 200 nm, a distance comparable to their width. The data for water is not shown as it was too noisy to extract a reliable slope. Indeed, it should be noted that the full range of hysteresis here corresponds to less than 1.5° and that the ability to measure such small variations due to the defects is in part due to the small and reproducible intrinsic hysteresis of the background surface, particularly when used with good solvents such as alkanes. The hysteresis measured with water is shown for barely sintered spheres in Fig. 3b, and still found to scale with n up to the highest concentrations. In this case, the detailed profile cannot be obtained by AFM due to tip effects and undercut, but we can approximate it by a spherical cap. This shape of defect pins the contact line more strongly and thus the hysteresis is significantly larger. The hysteresis also scales with n for the two alcanes (not shown in Fig. 3b but included in the summary Fig. 6), but the maximum concentrations tested were lower since the surfaces became perfectly wetting at concentrations below $10\mu\text{m}^{-2}$. Figure 3b shows that the advancing and receding angles both move away from the intermediate, equilibrium contact angle as the concentration increases. This has been observed in other studies with topographic defects[4–6] and can be interpreted by the fact that such defects have a bipolar force that is more wettable on one half and less wettable on the other (see Fig. 5 and Appendix A). In the case where the more and less wettable halves are nearly symmetric, then the force averaged over the surface is roughly null. This is in contrast to chemical defects, which usually have either a positive or negative force and therefore on average make the surface more or less wettable[30].

A hysteresis that scales with the concentration has been interpreted as defects acting independently to pin the contact line. If this is the case, the slopes in Fig. 3 give the energy dissipated as the contact line jumps over a single defect. The values of H/n are given in each figure. For the case of barely sintered spheres and decane, the slope is $\approx 4.10^4\, k_B T$, which is of the same order as the energy barrier estimated in Section 2.1. The slopes are at least an order of magnitude smaller in the case of the sintered spheres and

still no change in the dynamics is observed.

3.3 Hysteresis and defect shape

Next, we prepared a series of samples with nominally the same defect concentration, but sintered at 10 different temperatures. Defect profiles were obtained by AFM for each sample. Figure 1c shows 2 examples. A mean defect height ranging from $h_0 = 4.2 \pm 0.6\,\text{nm}$ to $74.1 \pm 1.0\,\text{nm}$ was determined from the detailed image analysis of typically 20 defects per sintering temperature. AFM yields accurate height data, but profile information can require interpretation due to possible tip-convolution effects and the inability to image undercut structures such as the bottom half of a sphere. These effects are most important for barely sintered defects. For final defect heights below 30 nm, the measured profiles are well described by a Gaussian

$$z = h_0 \exp\left[-\frac{x^2+y^2}{2d^2}\right], \tag{5}$$

where we refer to $2d$ as the width and h_0 as the height. The maximum slopes are less than 20° and the convolution with the AFM tip of radius order 5 nm introduces only a small error in the overall defect width, which ranges from 80 to 200 nm.

The hysteresis was measured on each surface using two alcanes, as before. Knowing that $H \propto n$ from the experiments described above, an energy dissipated per defect was found for each shape by subtracting the reference substrate hysteresis and normalizing by the concentration $n = 5.9 \pm 0.2\,\mu\text{m}^{-2}$. Figure 4 shows the dissipated energy as a function of the defect height. It ranges from $10^5\ k_\text{B}T$ down to $250\ k_\text{B}T$. In order to interpret the dependence on the shape, we first briefly recall the ideas that lead to the scaling expression for the hysteresis that is often quoted in experimental papers.

In a static picture, the shape that a contact line takes in the vicinity of a single defect depends on the balance between the pinning force of the defect and the elastic restoring force of the contact line. In the picture of Joanny and de Gennes, hysteresis arises because the force balance is multistable: there are multiple, locally stable energy minima and the specific configuration that the contact line adopts depends on the direction in which it is moving. They developed expressions for both forces applicable to a single defect and propose a graphical solution to the balance, like that shown in Fig. 5a. Figure 5b shows the sequence of solutions for an advancing and for a receding contact line, and the shaded area is the total energy dissipated as the contact line moves back and forth over one defect. Assuming that defects act independently, this area is H/n. They introduced the notion of *weak* and *strong* defects to refer to defects that are monostable and those that are multistable. Here we use the terminology *very strong* to signify that the defect force is at some points much much steeper than the elastic restoring force (in the coordinates plotted in Fig. 5). In this limit the shaded areas are nearly triangular, and consequently the hysteresis scales as

$$H = n\frac{\left(F_\text{d}^\text{max}\right)^2}{k}, \tag{6}$$

where F_d is the defect force and k is the Hookean spring constant of the contact line. The spring constant can be written [1]

$$k = \frac{\gamma \sin^2\theta_\text{eq}}{\ln(L/d)}, \tag{7}$$

where d is of order of the size of the defect and L is a large scale cutoff often taken as the capillary length or the size of a drop. Equation 6 has often been used to interpret experimental data [2,4–6,8,31]. In the case of Gaussian defects, the maximum defect force can be written (see Appendix A)

$$F_\text{d}^\text{max} = \sqrt{2\pi}\gamma e^{-1/2}\sin\theta_\text{eq} h_0. \tag{8}$$

According to eqn 6 the hysteresis therefore scales as

$$H = 2\pi e^{-1}\ln(L/d)\,\gamma {h_0}^2 n. \tag{9}$$

The same dependence, with a different numerical prefactor, can be found for spherical-cap shaped defects.

For these shapes, the defect width does not enter into the estimate for H when assuming *very strong* defects. So, tip convolution errors do not enter. Returning to Fig. 4, a hysteresis that scales as the square of the defect height agrees with the experimental data. The full range of defect sizes are shown here, spanning nearly 3 orders of magnitude in H/n, with the most sintered spheres yielding $250\ k_\text{B}T$.

3.4 Hysteresis summary

Equation 9 also gives a prediction for the scaling with the other parameters: the concentration of defects and the liquid. Figure 6 shows the experimental hysteresis (rescaled by the surface tension and with the hysteresis of the reference surface subtracted) as a function of $n{h_0}^2$ for all liquids, defect shapes and concentrations used in this study.

In the case of the defect concentration, in addition to the direct proportionality to n, the large-scale cutoff L can depend on the average spacing between defects [1]. Since we find $H \propto n$ for any given shape, we may argue that we are not sensitive to this variation, which appears as a logarithmic factor. It would nonetheless be perilous to attempt to extract the $\ln(L/d)$ from Fig. 6 since it depends highly on the prefactor of the scaling relation.

In the case of varying the liquid, both γ and θ_eq are changed. For strong defects, the angle dependence of the defect force and of the elastic force cancel, leaving a hysteresis proportional to the surface tension. It is already clear in Fig. 3a —which shows the normalized hysteresis— that there subsists a weak dependence on the contact angle, which is roughly 15° in the case of decane and 33° for hexadecane. This is seen again in Fig. 6 where hexacane data lies consistently above decane data. Such a liquid-dependence has been observed by others [6], who proposed the possibility of the emergence of a correlation length along the contact line and collective effects. We return to collective effects below, but here we note that an alternative possibility valid even for defects acting independently: as can be seen from geometrical arguments, for defects that are multistable but are not *very strong* according to the terminology introduced in the previous section,

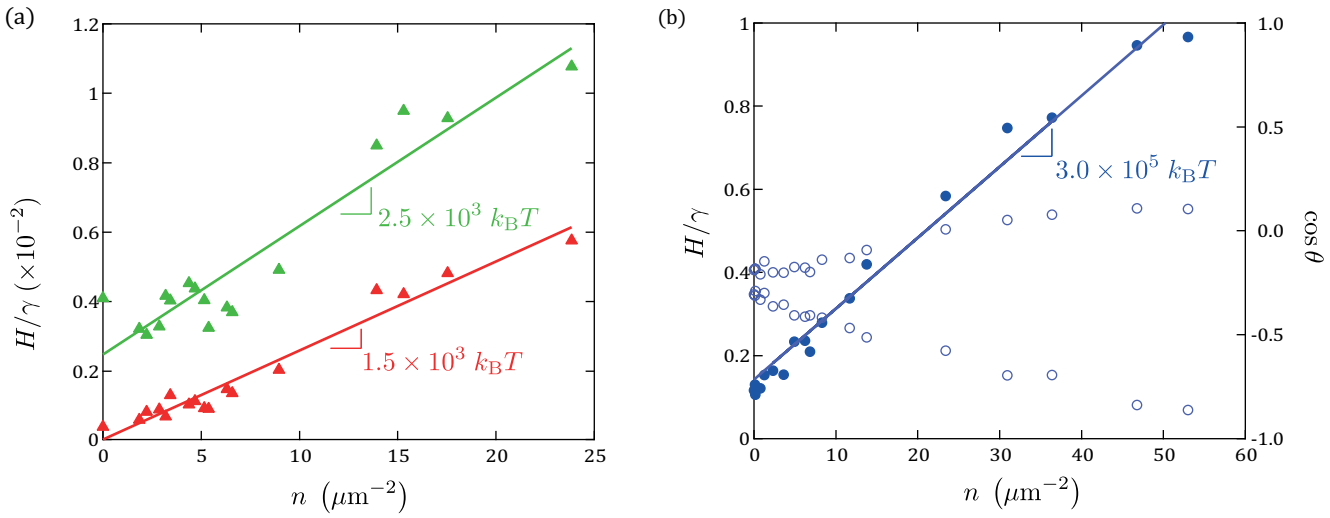

Fig. 3 Hysteresis as a function of the defect concentration (a) for heavily sintered defects with the profile shown in Fig. 1 (1164 °C, $h_0 = 6.3$ nm) and (b) for nearly unsintered defects (1080 °C, $h_0 = 74.1$ nm). For the latter, the open symbols indicate the advancing and receding angles. Three different liquids are used: decane (red), hexadecane (green) and water (blue). The linear slopes are indicated and give the energy dissipated per defect, H/n.

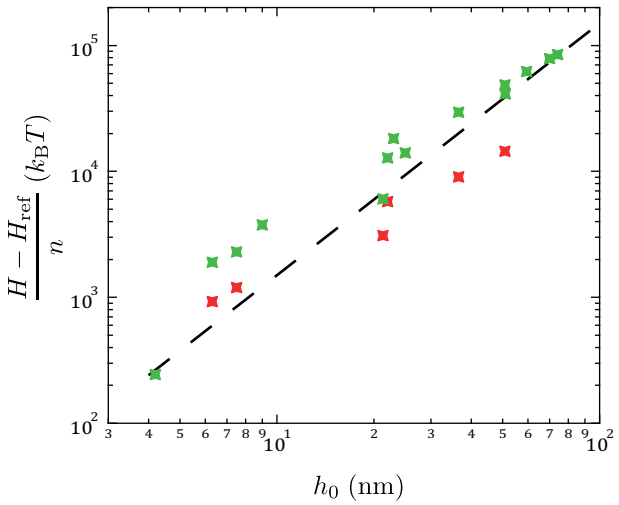

Fig. 4 Energy dissipated per defect as a function of the defect height as measured by AFM, for decane (red) and hexadecane (green). The dashed black line indicates the power law $h_0{}^2$.

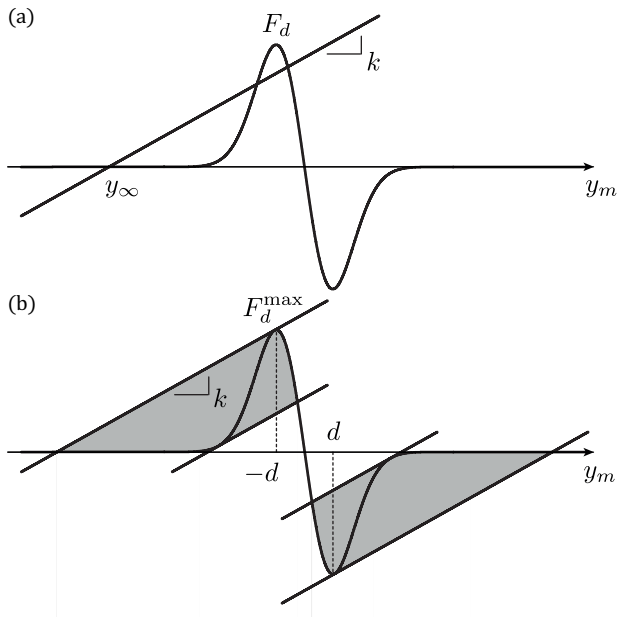

Fig. 5 Graphical method of solving the force balance according to Ref.[1] for a defect force F_d corresponding to a topographical bump and a Hookean elastic force corresponding to the line with slope k. (a) For some position of the contact line far from the defect (y_∞) there are two stable solutions (and one unstable) when the effective spring constant k of the contact line is not too stiff. (b) The grey areas represent the hysteresis energy over a single defect.

the shaded areas in Fig. 5 cannot be approximated by triangles and therefore depend on the details of the defect force F_d and not just on $F_d^{\max}$ as is assumed in eqn 6. In this case, the hysteresis still scales with γ but its dependence on θ_{eq} is not trivial and cases where it is not monotone can be found.

4 Discussion

The original aim of this study was to examine the relationship between the individual defects on a solid and the wetting properties on that surface. Despite having chosen the size range of defects with the explicit aim to measure thermal activation, we found no measurable effect on the slope of the low-velocity dynamics with any of the defects tested here. We propose two possible explanations. First, the visco-elastic dynamics on the PDMS surface treatment might dominate the dynamics and hide a regime of thermal activation. This idea can be tested by repeating this study with a different reference surface, one that still has a small intrinsic hysteresis. We have tried liquid-phase deposited organosilanes[32], and initial measurements have not found any difference in low-velocity slopes with or without defects of the same size as used in this study. A similar question arises however: do the thermally-activated dynamics already present on the silane dominate any possible thermal activation over additional defects? In other words, which scale is selected when there are multiple scales to the disorder? Another possibility is that the energy barriers to motion are much larger than estimated here, for example, if defects act collectively to pin the contact line and incremental motion thus requires overcoming a number of defects at a time.

We found that H scales linearly with n, which we have thus far discussed in the context of independent defects. Given the close proximity of defects for the high surfaces coverages used in this study, it is reasonable to expect that the range of action of neighboring defects should overlap. It has long been understood that collective effects can play a role in the hysteresis and one can ask if this linearity necessarily implies that defects act independently or if it can also be found for interacting defects.

In their simulation, Crassous and Charlaix focused on random, strong defects and found a sub-linear dependence[3], which had been observed by others[9]. There is no evidence of sub-linearity in our present study. The data in Crassous and Charlaix also crosses into the regime of weak defects, but no scaling is explicitly given. By definition, a single weak defect does not pin the contact line, however, a collection of random defects that are individually weak can also act collectively. The contact line exhibits a coherence length (or Larkin length) over which a number of defects act cooperatively to pin the line and multi-stability emerges where there was none for a single defect. Provided that the coherence length does not exceed the capillary length, Robbins and Joanny showed that there is always a hysteresis, even for vanishingly weak defects[33]. Their expression reduces to a linear dependence on defect concentration[34], and in particular gives the same scaling as eqn 9 for the case of Gaussian defects (see Appendix B). Therefore, Fig. 6 shows that experimental data follows this scaling, but this scaling does not discriminate which regime applies to the present study, ie. strong independent or weak collective pinning.

An advantage of the work presented here is that we have access to detailed defect information and can modify it to access a wide range of shapes, and, potentially, regimes. For example, we can attempt to answer the question whether individual defects are weak or strong by using the shape information to esti-

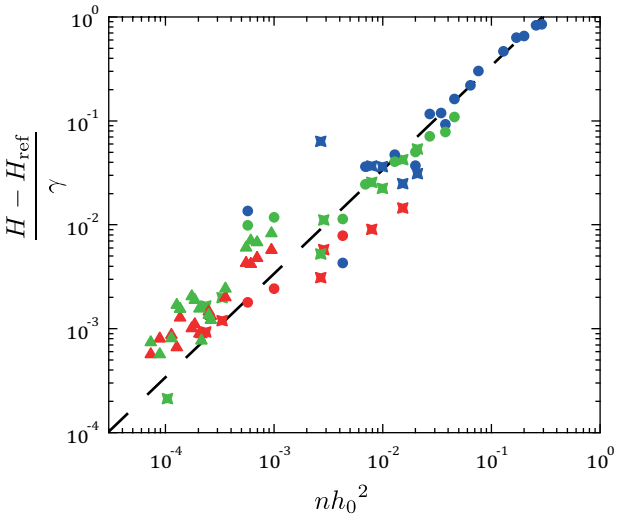

Fig. 6 Measured increase in rescaled hysteresis due to the presence of defects as a function of the scaling of eqn 9 for all of the combinations of defect density and shape tested here (nearly unsintered (circles), varying degrees of sintering (stars) and the very sintered shape already shown in Fig. 3a (triangles)) and three different liquids (decane (red), hexadecane (green) and water (blue)).

mate the defect force (see eqn 12) and compare it to the effective spring constant (eqn 7). For the smaller defects used (such as the blue curve in Fig. 1c) the defects are not *very strong*. Given the plausible range of the $\ln(L/d)$ factor it is not certain that they are even strong at all, but may indeed be at the limit of being weak. Measuring a contact angle hysteresis on individually weak defects raises the question of the physical origin of this hysteresis: is it due to a multistability that emerges due to collective pinning, as outlined above, or is the problem still monostable and the hysteresis is evidence of a force-threshold that is present in a force-driven situation, as we recently found in the case of an effective energy landscape [18]?

5 Conclusions

Wetting hysteresis —and more recently dynamics— in the presence of disorder or defects has been studied for some decades now. However, experiments linking the measurable surface properties and the wetting properties were lacking. By controlling the shape and concentration of defects and using a reference surface with well-characterized dynamics, we have made a step along this path. We find a simple scaling of the hysteresis but argue that it does not allow discrimination between models, thus illustrating that there is still considerable room to improve our understanding of which limits or physical conditions drive hysteresis for a given real actualization of the disorder. For example, are the individual defects weak or strong, do they pin the line independently or collectively, and is the problem monostable or multistable? In the case of dynamics, we show that there is no evidence of thermal activation on *added* defects, which we suggest may be due to another length scale emerging to determine the activation length. Numerical simulations that match the experimental defect properties are needed to further address these questions. One could thus control the transition of weak to strong pinning, investigate the passage from a single defect to a density of randomly-spaced defects and look for signatures of collective behavior such as the dependence on n and avalanches, in addition to simulating thermal-activation.

Appendix A

Here we justify the expression for the defect force in eqn 8. We begin by recalling that the local force on the contact line arises from the fluctuating part of the spreading parameter. For topographical defects and in the case of small slopes, this can be approximated as [1]

$$h(x,y) = -\gamma \sin\theta_{\rm eq} \frac{\partial z}{\partial y}, \tag{10}$$

where $z(x,y)$ is the surface profile, y is the direction of motion and x is transverse to this (parallel to the unperturbed contact line). We are interested in the total force integrated along the contact line, which can be approximated as [1]

$$F_d = -\int_{-\infty}^{\infty} \gamma \sin\theta_{\rm eq} \frac{{\rm d}z}{{\rm d}y}\Big|_{y=\psi(x)} {\rm d}x. \tag{11}$$

Here $\psi(x)$ indicates that the y coordinate is to be evaluated at the distorted contact line position. In other words, the problem is recursive since the force depends on the precise position of the contact line and the position of the contact line depends on the force. Following Joanny and de Gennes, we assume that the integral is dominated by the maximum force, when the deformation is near its maximum and the y coordinate is denoted y_m. For the Gaussian shape defined in eqn 5 the force can then be written

$$F_d = \sqrt{2\pi}\gamma \sin\theta_{\rm eq} \left(\frac{h_0}{d}\right) y_m \exp\left(\frac{-{y_m}^2}{2d^2}\right). \tag{12}$$

This gives the bimodal defect force illustrated in Fig. 5. The maximum force occurs at $y_m = d$ and yields eqn 8.

Appendix B

Here we recall the results of Ref. 33 for the hysteresis due to collective pinning of a contact line over a randomly disordered

solid and show that in our case it gives the same scaling as eqn 9. They find that the threshold force for depinning the contact line is

$$H \sim \frac{\overline{h}^2}{\gamma \sin^2 \theta_{\mathrm{eq}}}, \tag{13}$$

where $\overline{h}$ is the r.m.s. of the fluctuating part of the spreading parameter, given in eqn 10 for topographical defects. For Gaussian defects, and provided that the defects are not overlapping, this can be written as $\overline{h} = \sqrt{\pi/2}\gamma \sin\theta_{\mathrm{eq}} h_0 \sqrt{n}$, yielding

$$H \sim \gamma {h_0}^2 n. \tag{14}$$

Conflicts of interest

There are no conflicts to declare.

Acknowledgements

The authors gratefully acknowledge discussions with Etienne Rolley, Bruno Andreotti and Eugene Choi and technical assistance from the ENS support staff: José Palomo, Michael Rosticher, Carlos Domingues Gonçalves and José Da Silva Quintas. This work was funded by the ANR grant REALWET.

Notes and references

1 J.-F. Joanny and P.-G. de Gennes, *J. Chem. Phys.*, 1984, **81**, 552–562.

2 M. Delmas, M. Monthioux and T. Ondarçuhu, *Phys. Rev. Lett.*, 2011, **106**, 136102.

3 J. Crassous and E. Charlaix, *EPL*, 1994, **28**, 415.

4 S. M. M. Ramos, E. Charlaix, A. Benyagoub and M. Toulemonde, *Phys. Rev. E*, 2003, **67**, 031604.

5 S. Ramos, E. Charlaix and A. Benyagoub, *Surface Science*, 2003, **540**, 355 – 362.

6 S. Ramos and A. Tanguy, *Eur. Phys. J. E*, 2006, **19**, 433–440.

7 M. Ramiasa, J. Ralston, R. Fetzer and R. Sedev, *J. Phys. Chem. C*, 2012, **116**, 10934–10943.

8 M. Ramiasa, J. Ralston, R. Fetzer, R. Sedev, D. M. Fopp-Spori, C. Morhard, C. Pacholski and J. P. Spatz, *J. Am. Chem. Soc.*, 2013, **135**, 7159–7171.

9 J.-M. D. Meglio, *EPL*, 1992, **17**, 607.

10 M. Reyssat and D. Quéré, *J. Phys. Chem. B*, 2009, **113**, 3906–3909.

11 S. Semal, T. D. Blake, V. Geskin, M. J. de Ruijter, G. Castelein and J. De Coninck, *Langmuir*, 1999, **15**, 8765–8770.

12 M. Voué, R. Rioboo, M. H. Adao, J. Conti, A. I. Bondar, D. A. Ivanov, T. D. Blake and J. De Coninck, *Langmuir*, 2007, **23**, 4695–4699.

13 E. Rolley and C. Guthmann, *Phys. Rev. Lett.*, 2007, **98**, 166105.

14 K. Davitt, M. S. Pettersen and E. Rolley, *Langmuir*, 2013, **29**, 6884–6894.

15 P. Petrov and I. Petrov, *Langmuir*, 1992, **8**, 1762–1767.

16 R. Golestanian and E. Raphaël, *Phys. Rev. E*, 2001, **64**, 031601.

17 H. Perrin, R. Lhermerout, K. Davitt, E. Rolley and B. Andreotti, *Phys. Rev. Lett.*, 2016, **116**, 184502.

18 H. Perrin, R. Lhermerout, K. Davitt, E. Rolley and B. Andreotti, *Soft Matter*, 2018, **14**, 1581–1595.

19 R. Lhermerout, H. Perrin, E. Rolley, B. Andreotti and K. Davitt, *Nat. Commun.*, 2016, **116**, 12545.

20 T. D. Blake and J. M. Haynes, *J. Colloid Interface Sci.*, 1969, **30**, 421–423.

21 N. V. Venkataraman, C. V. Cremmel, C. Zink, R. P. Huber and N. D. Spencer, *Micropatterning in Cell Biology Part A*, Academic Press, 2014, vol. 119, pp. 91 – 121.

22 C. Huwiler, T. P. Kunzler, M. Textor, J. Vörös and N. D. Spencer, *Langmuir*, 2007, **23**, 5929–5935.

23 We have done this by comparing to defects with the same shape but covered with an organosilane monolayer instead of PDMS. The latter is susceptible to swell and potentially modify topography, particularly at sharp corners, whereas the former is not. We find that the hysteresis scales in the same way for both, apart from a factor attributable to their difference in contact angle.

24 J. W. Krumpfer and T. J. McCarthy, *Langmuir*, 2011, **27**, 11514–11519.

25 D. F. Cheng, C. Urata, B. Masheder and A. Hozumi, *J. Am. Chem. Soc.*, 2012, **134**, 10191–10199.

26 R. Lhermerout, *Theses*, PSL Research University, 2016.

27 J. J. Jasper, *J. Phys. Chem. Ref. Data*, 1972, **1**, 841–1010.

28 *CRC Handbook of Chemistry and Physics, 68th Edition*, ed. R. C. Weast, CRC Press, 1987.

29 *CRC Handbook of Chemistry and Physics, 90th Edition (CD-ROM Version 2010)*, ed. D. R. Lide, CRC Press, Boca Raton Florida, 2010.

30 V. de Jonghe and D. Chatain, *Acta Metallurgica et Materialia*, 1995, **43**, 1505 – 1515.

31 J.-M. di Meglio and D. Quéré, *EPL*, 1990, **11**, 163.

32 L. M., B. O., K. M., H. H., F. R., P. M., S. R. and J. K., *Surface and Interface Analysis*, **47**, 557–564.

33 M. O. Robbins and J. F. Joanny, *EPL*, 1987, **3**, 729.

34 D. Bonn, J. Eggers, J. Indekeu, J. Meunier and E. Rolley, *Rev. Mod. Phys.*, 2009, **81**, 739.